Convective Cloud Information derived from Himawari-8 data

SUMIDA Yasuhiko*, SUZUE Hiroshi*, IMAI Takahito**, and SOBAJIMA Akira***

Abstract

Himawari-8, which started operation on July 7 2015, carries Advanced Himawari Imager (AHI) - a state-of-the-art visible infrared radiometer that performs full-disk observation at 10-minute intervals and Japan area observation at 2.5-minute intervals simultaneously. The Meteorological Satellite Center of Japan Meteorological Agency (MSC/JMA) has developed Convective cloud information (CCI) derived from the high temporal resolution data produced by this Japan area observation. The product identifies three detection areas, rapidly developing cumulus areas (RDCAs), cumulonimbus areas (CBs), and dense anvil cirrus areas (mid/low cloud unknown areas; MLUAs) to support aviation safety. This report details the detection algorithms of each component of CCI.

1. Introduction

Convective Cloud Information (CCI) provides analysis for monitoring and nowcasting of convective cloud using Himawari-8 (Bessho et al., 2016) Rapid Scan Operation (RSO) data. The product is intended to support aviation safety by identifying rapidly developing convective cloud before weather radar or other observations detect precipitation.

Nowcasting based on geostationary meteorological satellite data from RSO is conducted by various meteorological organizations around the world. An example of RSO usage to detect developing cumulus is seen in the Convective Initiation (CI) product developed for the Geostationary Operational Environment Satellite – R series (GOES-R) (Mecikalski and Bedka, 2006) and the Meteosat Second Generation (MSG) (Siewert et al., 2010). Meteorological Satellite Center (MSC) of Japan Meteorological Agency (JMA) previously ran RSO at 5-minute intervals using the Multi-functional Transport Satellite -1R (MTSAT-1R), which served as backup to MTSAT-2, to monitor convective clouds during summer. MTSAT-1R RSO focused only on Japan and its vicinity while Full Disk (FD) operations were paused. In 2012, MSC/JMA began to provide a product called Rapidly Developing Cumulus Areas (RDCAs) (Okabe et al., 2011) derived from MTSAT-1R RSO data. However, RDCA was provided only in the daytime during summer due to MTSAT-1R's operational limitations.

Himawari-8 carries a state-of-the-art visible infrared radiometer, Advanced Himawari Imager (AHI). AHI performs ongoing observation of the Japan area at 2.5-minute intervals during FD observation, whereas FD observation was paused during MTSAT-1R's RSO. AHI also has 16 observation bands as compared to 5 bands of MTSAT series imagers. CCI takes advantage of high temporal and multi-spectral observations to identify cumulus and cumulonimbus forms likely to bring thunderstorm all day and night.

In this document, Chapter 2 gives an outline of the CCI

*System Engineering Division, Data Processing Department, Meteorological Satellite Center

**Office of Observation Systems Operation, Observation Department, Japan Meteorological Agency

***Forecast Division, Forecast Department, Japan Meteorological Agency

(Received September 16, 2016, Accepted December 14, 2016)

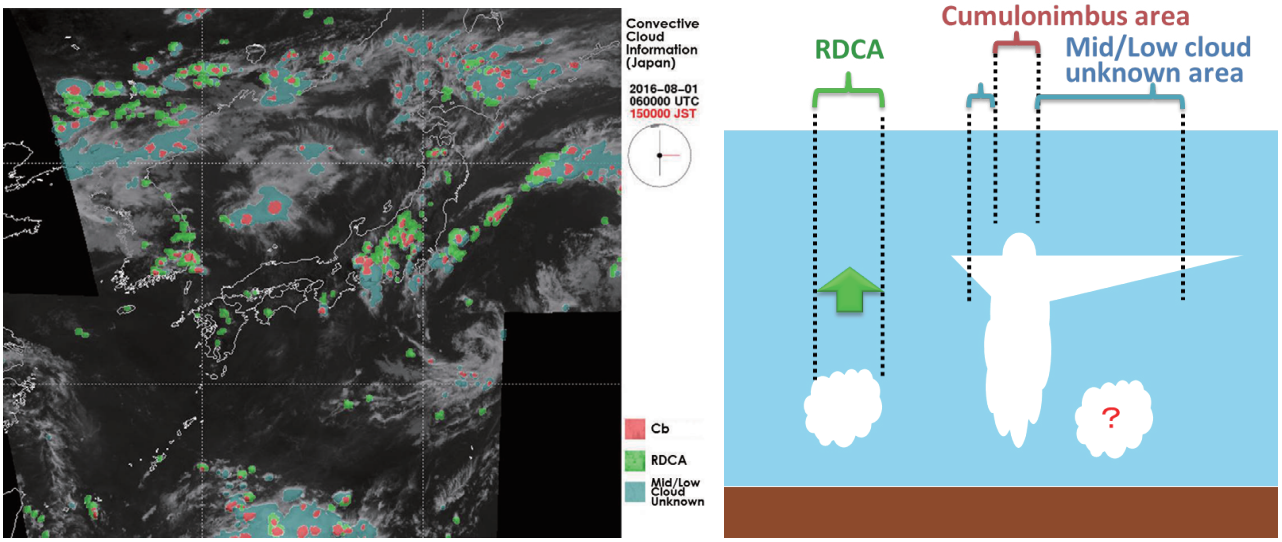

Fig. 1 Sample imagery for convective cloud information (left) and conceptual image of detection areas (right).

product and the data utilized for it , Chapter 3 describes the RDCA algorithms, Chapter 4 explain cumulonimbus areas (CBs) and mid/low cloud unknown areas (MLUAs), Chapter 5 presents case studies, and Chapter 6 gives the conclusion.

2. Overview of CCI product

The CCI detection areas are RDCA, CB and MLUA. Each detection area is displayed together in the background of Band 13 (10.4 μm) infrared imagery in CCI. MLUA is colored aqua, RDCA is green and CB is red, with overlaying in this order. Fig. 1 shows a CCI image and outlines the detection concept. Areas of cloud that could cause turbulence, lightning and other adverse conditions are considered hazardous to aviation operators. RDCA enables monitoring of cumulus which could potentially evolve into airmass thunderstorm within an hour. Mature cumulonimbus consists of two parts of cloud area; vertically developing thick cloud and dense anvil cirrus. The former is detected as CB and the latter as MLUA. During the mature and decaying phase, dense MLUA cloud areas hinder identification of low- or mid-level clouds below from AHI observation. RDCA detection is processed separately from CB and MLUA, and the algorithms used are described each.

Table 1 Himawari-8/AHI specifications and wavelengths used for the CCI.

Himawari-8				
Band #	Spatial Resolution	Central Wavelength	RDCA	Cb/MLUK
01	1 km	0.47 μm		
02		0.51 μm		
03	0.5 km	0.64 μm	○	○
04	1 km	0.86 μm		
05	2 km	1.6 μm		
06		2.3 μm		
07		3.9 μm		
08		6.2 μm	○	
09		6.9 μm		
10		7.3 μm	○	
11		8.6 μm	○	
12		9.6 μm		
13		10.4 μm	○	○
14		11.2 μm		
15		12.4 μm	○	○
16		13.3 μm	○	

2.1 Himawari-8 RSO

Himawari-8 was launched on October 7, 2014 and started operation on July 7, 2015 as the successor to the MTSAT series. AHI carried by Himawari-8 has the capacity of multi-spectral (16 bands) and higher spatial resolution in observation than the MTSAT series. Table 1 shows AHI specifications and the bands utilized for CCI. The AHI improves the frequency of observation dramatically, with the Japan area observed at 2.5-minute

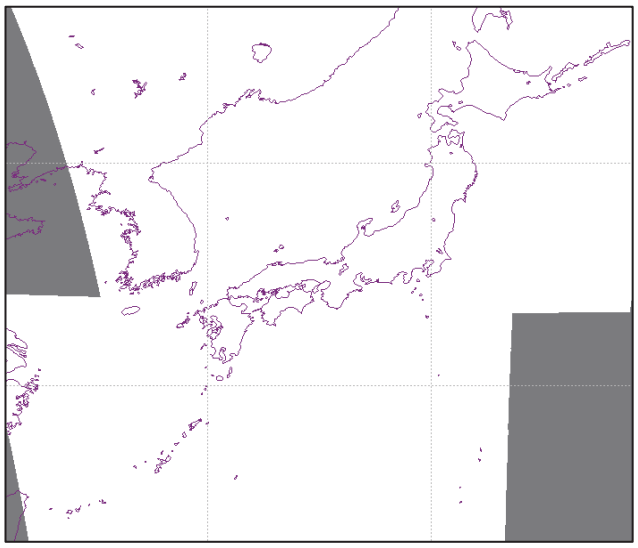

Fig. 2 Domain of Japan area observation by Himawari-8/AHI (white area).

intervals simultaneously even during FD scanning at 10-minute intervals. However, the CCI derived from this Japan area observation are processed every five minutes due to computing resource limitations. Fig.2 shows the domain of Japan area observation. The resolution of this product is based on 0.1-degree grid squares for RDCA and 0.04-degree grid squares for CB and MLUA.

2.2 Image pre-processing

Band 03 (0.64 μm) reflectivity is pre-processed with solar zenith angle correction in equation (1) below.

$$\mathrm{R_{mod}}(\text{Band 03}) = \mathrm{R_{obs}}(\text{Band 03}) \times \frac{1}{\cos(\theta_{\mathrm{sol}})}, \quad (1)$$

where, R(Band 03) is Band 03 reflectivity, the suffixes "mod" and "obs" represent modified and observed values, respectively, and θ_{sol} is the solar zenith angle. Here, the term of Band 03 reflectivity refers to the modified value.

These products are calculated using time-series data from successive images. The time trend between two images is calculated in consideration of cloud motion. The details of cloud motion tracking can be found in Appendix A.

2.3 Additional utilized data

In RDCA identification, it is assumed that all "rapidly developing" cumuli are likely to bring lightning, and cloud areas with lightning within an hour are defined as truth data. Statistical analysis for RDCA involves the use of lightning detection data from the Lightning Detection Network System (LIDEN), which JMA operates at 30 airports in Japan. LIDEN data include the time, location and type of lightning; cloud-to-cloud (CC) and cloud-to-ground (CG) discharge, based on detection of lightning-generated radio waves every second. Lightning detection for both CC and CG is defined on a grid of the active cumulonimbus area. RDCA detection is performed for 0.1 degree grid squares every five minutes, and LIDEN-based lightning detection data for the last five minutes are accumulated on the same grid.

Detection for CB and MLUA involves the use of Numerical Weather Prediction (NWP) of JMA's Global Spectral Model (GSM) every three hours. Radiance profiles for each AHI band were simulated using the Radiative Transfer for the Television and Infrared Observation Satellite (TIROS) Operational Vertical Sounder (RTTOV) fast radiative transfer model (Eyre, 1991). As the horizontal resolution of NWP is 0.5 degree grid squares, the data are interpolated into 0.04 degree grid squares using the method outlined in Appendix B.

3. Rapidly developing cumulus area

Strong updrafts in developing cumulus cause cloud top growth, irregular texture at the cloud top surface and ice particle generation, and can therefore be monitored via RSO. RDCA detection involves the calculation of various indicators related to these features followed by determination of the possibility of thunderstorms in the next hour. Fig. 3 outlines the process of RDCA detection, highlighting the indicators used, the method of logistic regression (LR) and detection itself.

3.1 Detection indicators

Table 2 shows the detection indicators used for RDCA. Estimation for each is based on area-averaging, maximum/minimum and standard deviation, and on calculation domains within ±10, ±6 and ±10 grid squares, respectively. RDCA detection also involves switching

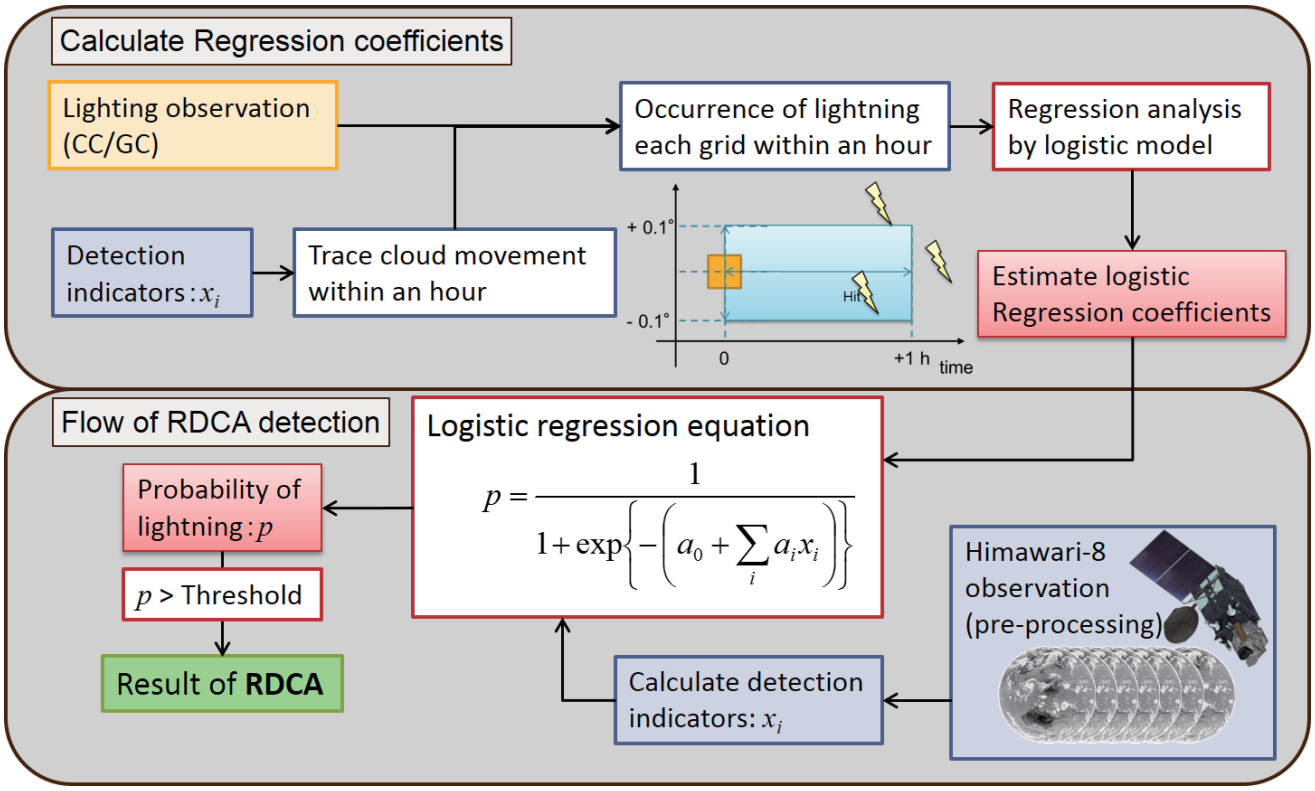

Fig. 3 RDCA processing

over the day/night indicators at a solar zenith angle of 75 degrees. At nighttime, the limitation of Band 03 reflectivity results in detection using only indicators from certain infrared bands (Band 08 - Band 16), and low-level cloud is occasionally missed.

Detection of cloud top roughness (No.1 - No.4)

The purpose of these indicators is to determine the characteristics of irregular texture at the top of cloud that develops vertically in the formative stage. The characteristics of indicators form Band 03 reflectivity and Band 13 brightness temperature (BT) may be similar, but differ in terms of solar incidence to the cloud surface and resolution (Band 03: 0.5 - 0.75 km, Band 13: 2.5 - 3 km around Japan). The indicators of the difference between maximum and area-averaging (No. 1) and standard deviation (No. 2) are derived from Band 03 reflectivity, and those of the difference between minimum and area-averaging (No. 3) and standard deviation (No. 4) are derived from Band 13 BT. The indicators for Band 03 cannot be used for nighttime detection ($\theta_{sol} > 75°$).

Detection of ice cloud (No.5 - No.7)

These indicators provide information on cloud phase and cloud top properties to discriminate cirrus, volcanic ash and deep convective cloud. All are calculated as the brightness temperature difference (BTD) in area-averaged fields. No. 5 represents the BTD between Band 16 (13.3 μm) and Band 13. As its characteristics differ between infant cumulus and mature cumulonimbus, it is considered one of the most important indicators in the detection of developing cumulus (Mecikalski and Bedka, 2006). No. 6 represents the BTD between Band 15 (12.4 μm) and Band 13, known as the “sprit window” technique. This indicator supports identification of convective rainfall areas (Inoue, 1987). No. 7 represents the BTD between Band 11 (8.6 μm) and Band 13 and allows discrimination between water cloud and ice cloud in cumulonimbus (Matthee and Mecikalski, 2013).

Water vapor detection above cloud top (No.8, No.9)

These indicators provide information on cloud top height location relative to the tropopause. BTD between

Table 2 RDCA Detection indicators.

No.	Parameter	Primary objective
1	Band 03 reflectivity: Maximum - Average	Detection of cloud top roughness Day time only
2	Band 03 reflectivity: Standard Deviation	
3	Band 13 BT: Minimum - Average	Detection of cloud top roughness
4	Band 13 BT: Standard Deviation	
5	Band 16 BT Average - Band 13 BT Average	Detection of ice cloud
6	Band 15 BT Average - Band 13 BT Average	
7	Band 11 BT Average - Band 13 BT Average	
8	Band 08 BT Average - Band 13 BT Average	Water vapor detection above cloud top
9	Band 10 BT Average - Band 08 BT Average	
10	Temporal Variation of Band 03 Reflectivity Average	Presumption of developing level of cloud Day time only
11	Temporal Variation of Band 13 BT Average	Presumption of developing level of cloud
12	Temporal Variation of Band 11 BT Average - Band 13 BT Average	Detection of developing ice cloud
13	Temporal Variation of Band 15 BT Average - Band 13 BT Average	

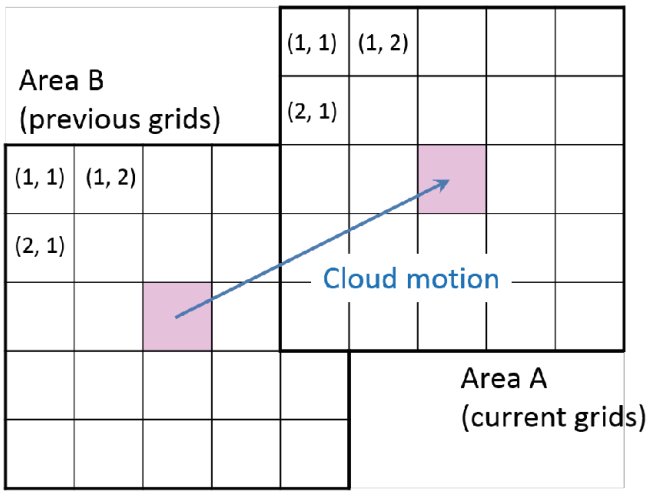

Fig. 4 Temporal variation of image averaging in grids.

water vapor bands (Band 08 - Band 10) and Band 13 for mature cumulonimbus is valued at near zero or positive, and the indicators give the degree of cumulonimbus maturity (Ackerman, 1996). No. 8 represents the BTD between Band 08 (6.2 μm) and Band 13 in area-averaged fields, and No. 9 represents the BTD of two water vapor bands between Band 08 and Band 10 (7.3 μm) in area-averaged fields.

Presumption of cloud development level (No.10, No.11)

Cloud motion is cancelled out using the tracking method outlined in Appendix A, and the indicators below are then used to estimate the time trend between two images. Here the template area size (t = 2) and the search area size (s = 3) are considered, and Band 13 BT fields transformed to 0.04-degree grid squares are used for cloud motion tracking. The area-averaged time difference is estimated by averaging the difference between detection area grids (21 × 21) in the current image "A" and the same grids with the center sifted by the amount of cloud motion in the previous image "B" (Fig. 4). The area-averaged time trend $\overline{\Delta x}$ is then given by

$$\overline{\Delta x} = \frac{1}{\mathrm{N}} \sum_i \sum_j \{x_A(i,j) - x_B(i,j)\}, \qquad (2)$$

where, x_A and x_B represent the physical parameters in image "A" and image "B", respectively, i and j represent indices of area-averaged grid squares and N is total number of grids in the template area.

No. 10 represents the temporal difference in Band 03 reflectivity. This indicator expresses optical depth increase caused by cloud growth, but cannot be used for nighttime detection ($\theta_{\mathrm{sol}} > 75°$). No. 11 represents the temporal difference in Band 13, allows estimating of cloud top height development.

Table 3 Elements and thresholds used in detection area discrimination (pre-processing).

Elements	Threshold	Comments
Band 13 BT	< 288.15 K	Filtering out clear region
Band 03 Reflectivity	> 0.45	Filtering out optically thin cloud Extractiong thick cloud
Band 13 - Band 15 BT differece	< 2.0 K	Filtering out thin and upper level cloud (cirrus)

Detection of developing ice cloud (No.12, No.13)

No. 12 and No. 13 represent time trend of BTD between Band 11 and Band 13 and that between Band 15 and Band 13, respectively. The area-averaged time trend of BTD is calculated using the method outlined in the previous sub-section after the BTD of each grid in each image is estimated. These BTDs relate to the cloud top phase as mentioned above, and their time trend helps to clarify the relationship between cloud development and ice cloud growth. However, these indicators make only a small contribution to RDCA detection due to the difficulty of precise time trend calculation.

3.2 RDCA candidate discrimination

This process is applied to discriminate the RDCA candidate from clear areas and thin upper-level cloud. The thresholds for discrimination are shown in Table 3.

Band 13 BT is used to remove clear area. Grids with BT values above the threshold are considered clear area and are eliminated from the RDCA candidate.

BTD between Band 13 and Band 15 can be used to remove thin cirrus. This method is adopted for cloud type discrimination in general, and leverages the characteristic that Band13 BT for upper-level cloud consisting of ice crystal is higher than Band 15 BT because of the former's low absorptivity of ice crystal (MSC/JMA 2000). Grids where BTD exceeds the threshold are recognized as cirrus and they are eliminated.

Optically thick cloud is also extracted for the RDCA candidate. This process eliminates thin cirrus area not eliminated by previously applied BTD method. Grids where reflectivity is less than the threshold are eliminated. The Band 03 reflectivity threshold cannot be used at nighttime ($\theta_{sol} > 75°$).

Fig. 5 shows the results of the discrimination process. Here, the process eliminates a fog area over northern Sea of Japan and upper-level cloud over western Japan.

Valid grids are defined as those not eliminated in discrimination process and all indicators are calculated.

3.3 Probability index based on logistic regression analysis

RDCA is estimated using a statistical model based on LR analysis (a non-linear multiple regression analysis). A

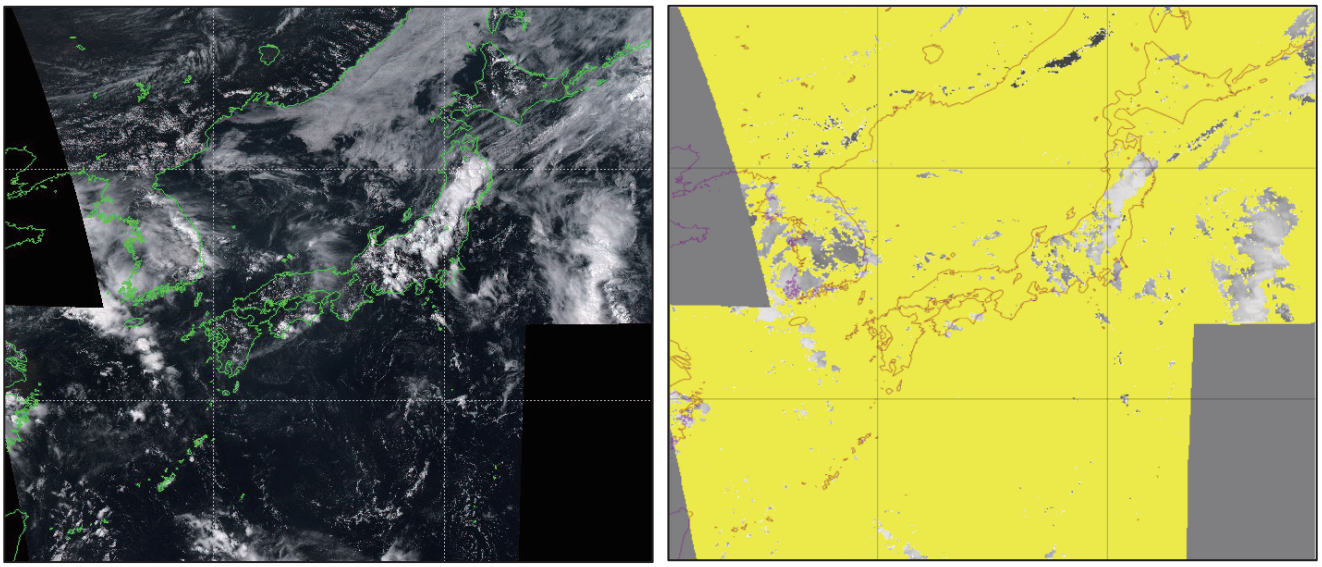

Fig. 5 VIS imagery (left) and candidate RDCA discrimination (right) at 4:30 UTC on August 2, 2015. Yellow areas are removed in preprocessing.

LR model is used to estimate the probability of lightning detection by LIDEN, resulting in values from zero (not detected) to one (detected). The LR function is given by

$$p = 1 \Big/ \left[1 + \exp\left\{ -\left(a_0 + \sum_i a_i x_i \right) \right\} \right], \qquad (3)$$

where, x_i represents an explanatory variable (based on the detection indicators described in section 3.1), a_0 and a_i are regression coefficients and i is the index of each detection indicators. The dependent variable p indicates the probability of lightning detection.

For LR analysis, the probability of lightning detection is determined in consideration of whether lightning is detected in the next 60 minutes within an area of 0.1 degrees around. This probability also is considered Band 13 BT cloud motion (Appendix A) during 60 minutes.

The parent population of each indicator for LR defines the set of grids calculable as explanatory variables during periods described below. These parent populations are also divided into three classes by BT;

① less than 250 K (high cloud)
② greater than or equal to 250 K and less than 273.15 K (middle cloud)
③ greater than or equal to 273.15 K and less than 288.15 K (low cloud)

The parent populations of each indicator and each class of BT are then separated into bins with the same number of samples. Daytime/nighttime detections are conducted separately because Band 03 reflectivity data are not available at nighttime.

Dominant airmass thunderstorms recorded from first to fifth of August, 2015 are using for the LR analysis. The periods are for four daytime hours from 03:00UTC to 07:00UTC (12:00 to 16:00 local time), and for three nighttime hours from 09:00UTC to 12:00UTC (18:00 to 21:00 local time) for each day. This helped to impose the strong sensitivity of these cases on the LR model and ensures determination with possible lead times. However, such an approach may result in reduced detection accuracy with developing cloud in large scale disturbances and frontal zones. There is a trade-off between accuracy and lead-time.

3.4 RDCA detection

The probability of lightning detection is calculated for 0.01-degree grid squares, while RDCA detection is 0.1 degrees (defined as “detection square” of 10 × 10). These data are processed to mitigate the uncertainty in cloud movement and indicator processing. An RDCA is determined if a detection square meets two conditions;

① The ratio of valid grids of the probability in the detection square exceeds 10 %.
② The average of the top 25 % of probability in the detection square exceeds $\mathrm{thr}^{\mathrm{RDCA}}$ (i.e., the threshold for detection given as 0.3).

Successive monitoring

RDCA may be detected falsely when thin upper-level cloud passes over low-level clouds, as such areas are erroneously regarded as growing rapidly and having increasingly irregular texture. By contrast, when an RDCA is detected correctly, the detection intends to be continued in subsequent images. Accordingly, verification process to ensure the continuity between successive two images is adopted. In particular, the probability index is calculated only within 0.1-degree grid around the grid of RDCA detected previously.

4. Cumulonimbus areas and mid/low cloud unknown areas

Cumulonimbus is a thick cloud area developing vertically. Its clouds resemble huge turrets in the early stage, then spread horizontally upon reaching the tropopause. Cloud spreading around the turret shape cloud is dense anvil cirrus. As the turret shape cloud results from strong updrafts, the AHI can observe the presence of updrafts at the cloud top surface as the local minimum of BT around the cloud area. Dense anvil cirrus areas have relatively weak disturbance at the cloud top, however RDCAs may be present below. Accordingly turret shape clouds (CBs) and dense anvil cirrus areas (MLUAs) are detected, and are depicted in the CCI image. As upper-level thick clouds without CB prevent the AHI from observing cumulus below, such cloud areas are also

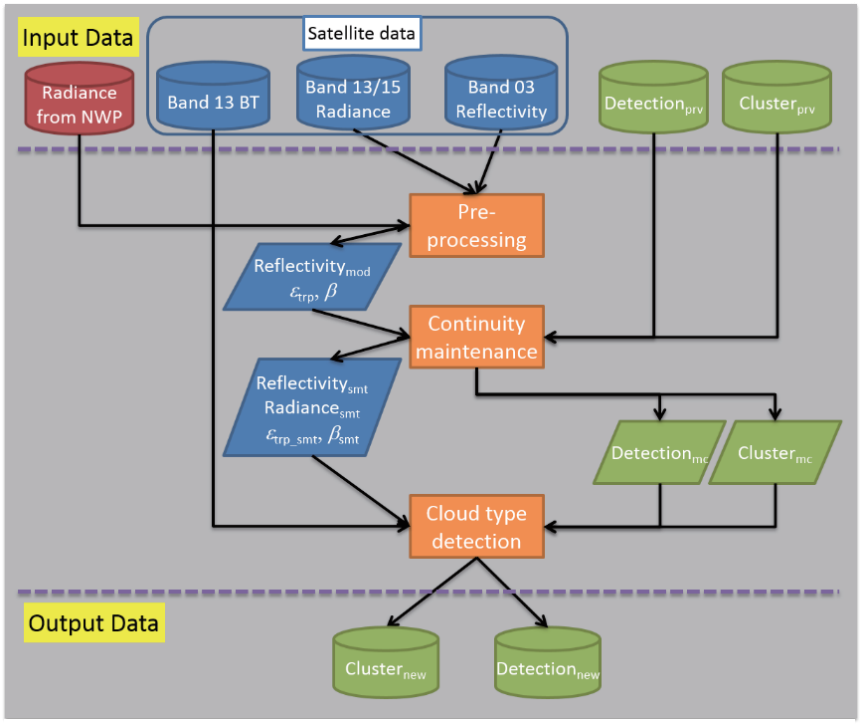

Fig. 6 CB and MLUA detection process flow. The suffixes "prv", "mod", "smt", "mc" and "new" represent previous detection data, solar zenith angle corrected data, smoothed data, motion cancellation data and new detection data, respectively.

identified as MLUA.

Fig. 6 shows the detection process for CB and MLUA. In pre-processing, visible images are corrected for the solar zenith angle and detection parameters are calculated. Cloud motion on various horizontal scales is then estimated in continuity maintenance process. Thick clouds are clustered as a spatial successive cloud area (cloud cluster), and the current cloud cluster is identified with the previous one. In the cloud type detection process, MLUAs are extracted as thick cloud areas reaching the tropopause among cloud clusters, and CBs are detected as a protrusion from MLUA. Results of CB and cloud cluster detection are kept for the next detection.

4.1 Detection parameters

Effective emissivity

The degree of transmission from clouds in radiance is estimated using effective emissivity. The radiance at wavelength λ that would be observed from a black body at the tropopause $I_{trp}(\lambda)$ and the radiance that would be observed in no cloud $I_{clr}(\lambda)$ are estimated from NWP vertical atmosphere profiles using the radiative transfer model mentioned in section 2.3. Then effective emissivity at the tropopause $\varepsilon_{trp}(\lambda)$ (Pavolonis, 2010) is defined as

$$\varepsilon_{trp}(\lambda) = \frac{I_{obs}(\lambda) - I_{clr}(\lambda)}{I_{trp}(\lambda) - I_{clr}(\lambda)}, \qquad (4)$$

where, $I_{obs}(\lambda)$ is the observed radiance at wavelength λ. $\varepsilon_{trp}(\lambda)$ can be considered as normalized BT. $\varepsilon_{trp}(\lambda)$ is equal to zero at the clear grid. By contrast, $\varepsilon_{trp}(\lambda)$ is equal to one at the grid filled with cloud reaching the tropopause. As the effects of atmospheric absorption and emissivity from ground are considered by the results of radiative transfer calculation, there is no need to change the threshold for different seasons or regions to enable discrimination between thick clouds and other clouds. However, only effective emissivity cannot be used to discriminate between upper-level thin cloud and low-level thick cloud.

$\varepsilon_{trp}(\lambda)$ is calculated at Band 13 for detection process and at Band 15 for estimating following optical thickness ratio.

Optical thickness ratio

This multi-band parameter is adopted to handle clouds that cannot be distinguished using effective emissivity. The optical thickness ratio $\beta(\lambda_1/\lambda_2)$ is defined as

$$\beta\left(\lambda_1/\lambda_2\right) = \frac{\ln[1-\varepsilon(\lambda_1)]}{\ln[1-\varepsilon(\lambda_2)]}. \qquad (5)$$

In this detection, the wavelengths λ_1 and λ_2 are assigned to Band 15 and Band 13, respectively. The value of $\beta(\text{Band 15}/\text{Band 13})$ is near one for black body-like clouds, greater than one for thin ice clouds, and less than one for volcanic ash and Asian dust. This relationship corresponds to that of BTD between Band 13 and Band 15. Accordingly, this parameter can be used to eliminate

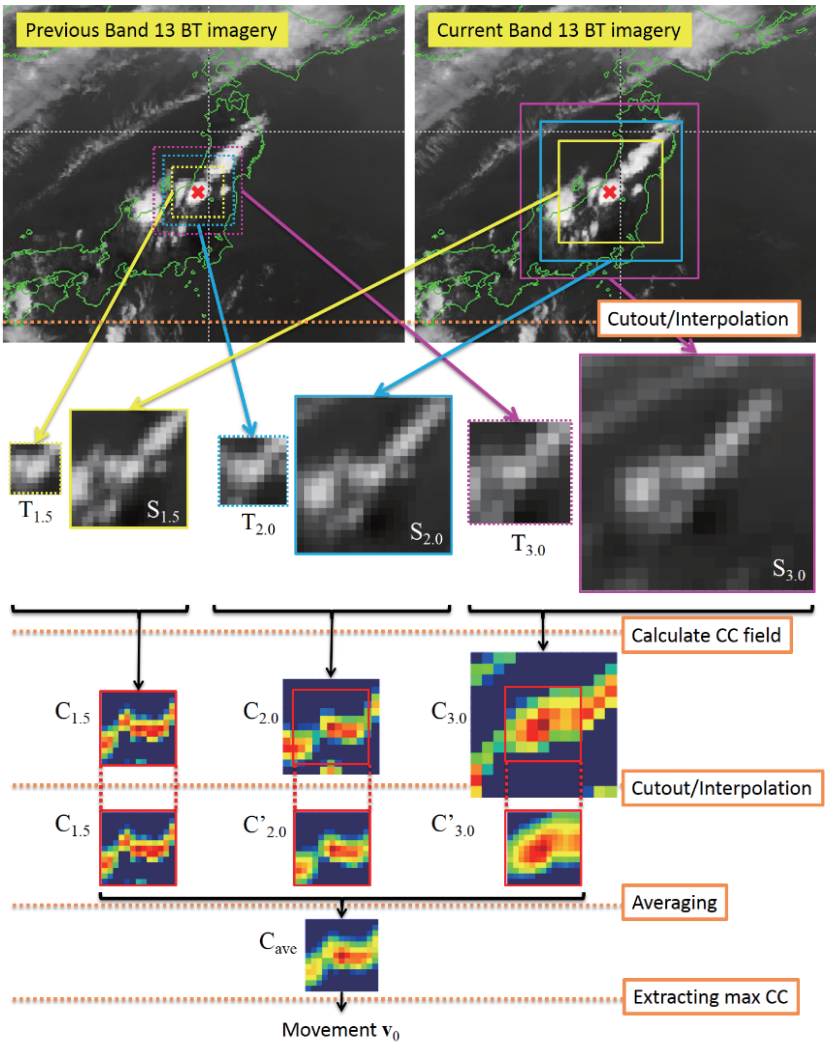

Fig. 7 Coarse matching process.

thin ice clouds corresponding to upper-level thin cloud areas.

4.2 Continuity maintenance

The cloud motion tracking for each grid is applied for the method outlined in Appendix A. This product has a template area size of t = 4 and a search area size of s = 6. However, it cannot track movement at speeds of less than 20 m/sec in five-minute interval image, as this method estimates the cloud movement in grid units (5 - 6 km around Japan). Accordingly, multi-level matching process (coarse matching and fine matching) is adopted for the cloud tracking to allow the handling of various cloud cluster sizes (cloud cluster detection is mentioned in Section 4.3). The tracking results are then utilized for image smoothing to maintain continuity. To reduce the burden on computer resources, this cloud tracking is processed for each cloud cluster.

Coarse matching

The movement of cloud areas containing one cloud cluster is roughly estimated. Here, imagery is cut out in several resolutions, cloud tracking is processed in each resolution, and then the multiple tracking results are averaged to improve matching accuracy (Fig. 7).

Three template sizes are decided depending on cloud cluster size. If the number of grids in a cloud cluster is “n” and the basic size L is determined as $1.5\sqrt{n}$, then Band 13 radiance fields I_{obs} are interpolated with 1.5L/(2t+1), 2.0L/(2t+1) and 3.0L/(2t+1) times resolution at the midpoint of the center of mass (CM) for each cloud cluster (L × L grids). If the cloud cluster is too small to be tracked (the size L is less than 4.5), I_{obs} is interpolated with 0.75, 1.0 and 2.0 times resolution, respectively. The interpolation method is shown in Appendix B. The correlation coefficient fields calculated by equation (A.4) for each resolution are defined as $C_{1.5}$, $C_{2.0}$ and $C_{3.0}$. The movement $v_0(\xi^{max}, \eta^{max})$ of coarse matching is finally estimated as the highest position of averaged correlation coefficient fields C_{ave} between $C_{1.5}$, $C_{2.0}$, and $C_{3.0}$. Here, as the correlation coefficient fields have different resolutions, the resolutions of $C_{2.0}$, and $C_{3.0}$ are made in the same as that of $C_{1.5}$ before averaging.

Fine matching

Next, the movement of the whole cloud cluster is estimated in fine matching (Fig. 8). The cloud motion of all grids (x_a, y_a) at the border of a cloud cluster is traced in Band 13 radiance field I_{obs}. After the center grid of the search area is re-positioned in consideration of the movement $v_0(\xi^{max}, \eta^{max})$ of coarse matching, the correlation coefficient (equation (A.4)) at the border is

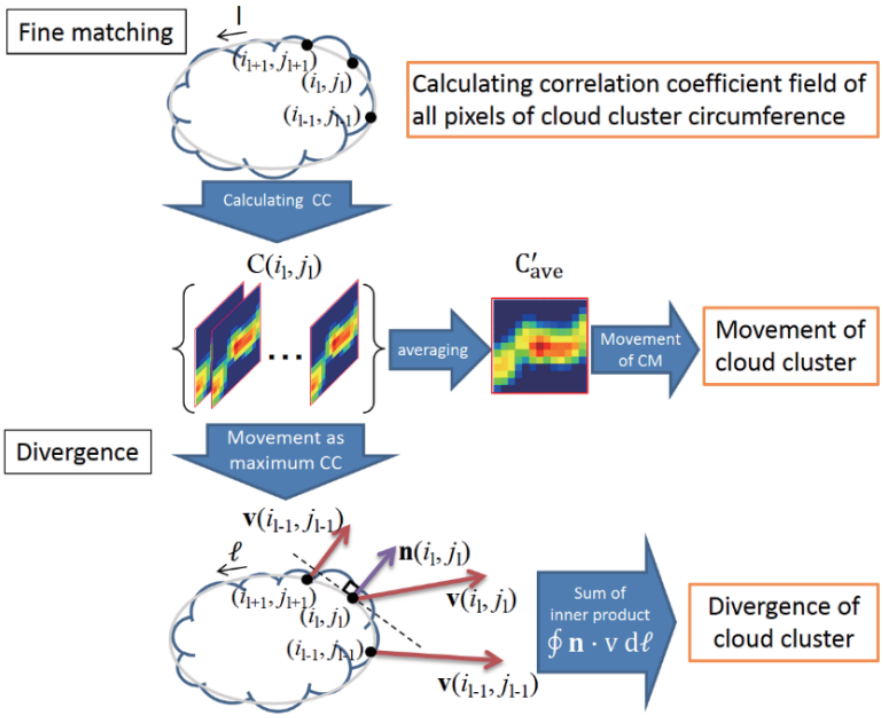

Fig. 8 Fine matching process.

calculated as $C_a(\xi,\eta)$. All correlation coefficients $C_a(\xi,\eta)$ are then averaged as

$$C'_{ave}(\xi,\eta)=\sum_{a} C_a(\xi,\eta);\ -s\le\xi\le s,-s\le\eta\le s. \quad (6)$$

The movement of cloud cluster v is set as the CM of $C'_{ave}(\xi,\eta)$ rather than as the position with the highest $C'_{ave}(\xi,\eta)$. This is because a higher correlation coefficient area is found at the border of a cluster, if the cloud cluster could spread radially. The movement of CM (ξ^{CM},η^{CM}) is given by

$$\xi^{CM}=\sum_{\xi=-s}^{s}\sum_{\eta=-s}^{s}\xi\cdot C'_{ave}(\xi,\eta)\Big/\sum_{\xi=-s}^{s}\sum_{\eta=-s}^{s}C'_{ave}(\xi,\eta),$$
$$\eta^{CM}=\sum_{\xi=-s}^{s}\sum_{\eta=-s}^{s}\eta\cdot C'_{ave}(\xi,\eta)\Big/\sum_{\xi=-s}^{s}\sum_{\eta=-s}^{s}C'_{ave}(\xi,\eta). \quad (7)$$

In addition, the divergence of each cloud cluster is estimated. Vector field $\boldsymbol{v}$ is defined as the position $(\xi_a^{max},\eta_a^{max})$ of the maximum correlation coefficient $C_a(\xi,\eta)$ in each grid (x_a, y_a) at the border, and normal vector to the border is **n**. Then divergence is given as

$$\mathrm{div(V)}=\oint \boldsymbol{v}\cdot\mathbf{n}\,d\ell, \quad (8)$$

where, $d\ell$ is a pieced length of the border. This divergence is used for CB detection (Section 4.4).

Image smoothing

Band 13 radiance, Band 03 reflectivity, effective emissivity and optical thickness ratio are smoothed temporally and spatially. The previous data $V_{obs}(1,x,y)$ are applied for motion cancellation data $V_{mc}(x,y)$ repositioned in consideration of the movement of CM. The current data $V_{obs}(2,x,y)$ and $V_{mc}(x,y)$ are stored in a three-dimensional array $V_{org}(t,x,y)$ as

$$V_{org}(1,x,y)=V_{mc}(x,y),$$
$$V_{org}(2,x,y)=V_{obs}(2,x,y). \quad (9)$$

The smoothed data are calculated using temporal-spatial weighted Gaussian filter as

$$V_{smt}(1,x,y)=\sum_{h=0}^{1}\sum_{i=-\ell}^{\ell}\sum_{j=-\ell}^{\ell}w(1,i,j)V_{org}(1+h,i+x,j+y)\Big/\sum_{h=0}^{1}\sum_{i=-\ell}^{\ell}\sum_{j=-\ell}^{\ell}w(1,i,j),$$
$$V_{smt}(2,x,y)=\sum_{h=-1}^{0}\sum_{i=-\ell}^{\ell}\sum_{j=-\ell}^{\ell}w(2,i,j)V_{org}(2+h,i+x,j+y)\Big/\sum_{h=-1}^{0}\sum_{i=-\ell}^{\ell}\sum_{j=-\ell}^{\ell}w(2,i,j),$$
$$w(t,i,j)=\exp\left[-\frac{\{mn(t)-mn(t-1)\}^2}{\sigma_t^2}-\frac{i^2+j^2}{\sigma_\ell^2}\right], \quad (10)$$

where, $\sigma_\ell=\ell=2$, $\sigma_t=16.7$, and $mn(t)$ represents the image clock time (in minute). The time difference between two images is 5 minutes. Fig. 9 shows Band 13 radiance imageries before and after image smoothing.

4.3 Cloud cluster detection

Thick cloud detection and CB candidate

In the cloud clustering process, cloud areas likely to retain the same tropopause level are grouped as a continuous cloud cluster. First, the extraction condition for thick cloud areas as components of a cloud cluster is given as

$$thr_3^{\varepsilon_{trp}}<\varepsilon_{trp}(\text{Band 13}) \text{ and } \beta(\text{Band 15/Band 13})<thr^{\beta}, \quad (11)$$

where, $thr_3^{\varepsilon_{trp}}$ and thr^{β} are detection thresholds (Fig. 10). The CB candidate is also extracted as

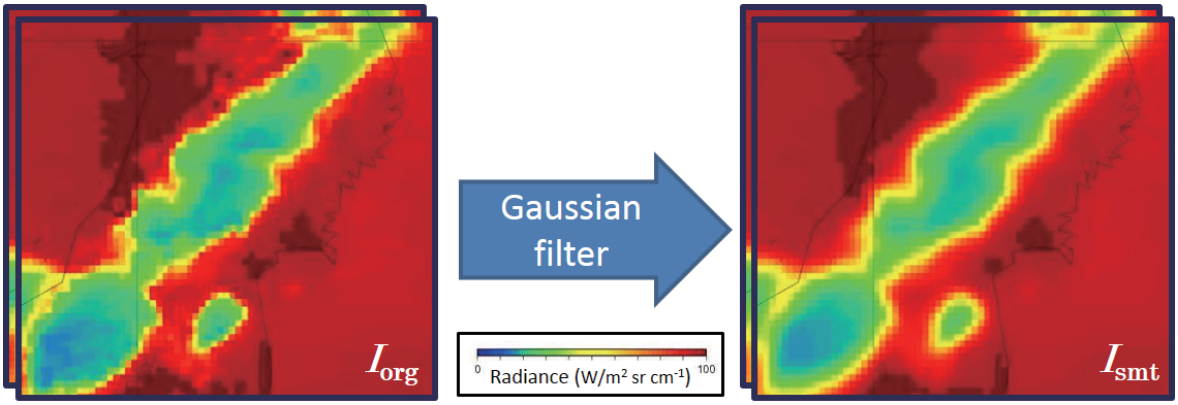

Fig. 9 Smoothing of radiance images based on Gaussian filtering in the temporal and spatial domains (left: original radiance fields, right: smoothed radiance fields).

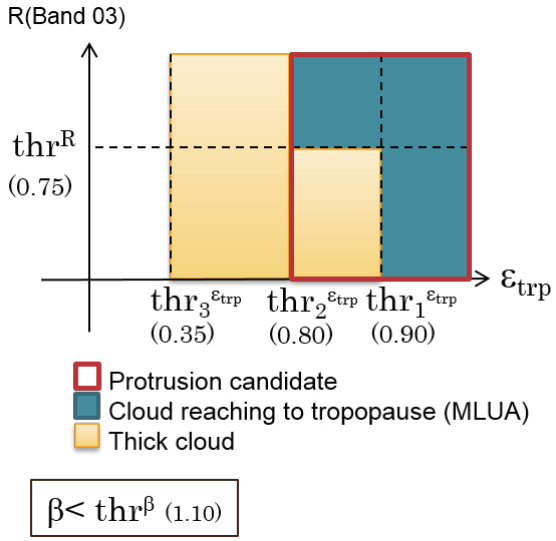

Fig. 10 Thresholds for cloud area discrimination and range of protrusion candidate.

$\mathrm{thr}_2^{\varepsilon_{trp}} < \varepsilon_{trp}(\text{Band 13})$ and $\beta(\text{Band 15/Band 13}) < \mathrm{thr}^{\beta}$, (12)

where, $\mathrm{thr}_2^{\varepsilon_{trp}}$ is the detection threshold (Fig. 10).

Cloud clustering

The border of each cloud cluster is marked by the "ridge" of Band 13 radiance field, and the local minimum of radiance is assumed to be at the center of each cloud cluster in the thick cloud area. Cloud clusters are detected by tracing the gradient of radiance (flow) in each grids, and grids reaching the same peak belong to a successive cloud cluster group. This results in cloud clusters that have a high thick cloud area at the center and low or thin cloud areas around them. Cloud clusters are cut out along low effective emissivity. The cloud clustering method is shown in Fig. 11. Here, a three-dimensional array $C^c(t,x,y)$ is allocated for reservation of the temporal cluster number. The final cluster number is assigned after cloud cluster identification process due to the need for consistency with the past image. A cloud cluster example is shown in Fig. 12.

Identification of cloud clusters with previous clusters

A current cloud cluster identified with the previous one can be given the same cluster number. The current cloud cluster that most closely fits with previous one in consideration of cloud motion is selected as identical (Zinner et al., 2008). The identification applies to the combination of cloud clusters for which the number "n" of common grids is the maximum. If the number of such grids is below 20 % in either cloud clusters, this identification is eliminated. If the difference vector between CM movement of identical clusters and tracking movement exceeds typical scale of cloud cluster $\sqrt{n}$ or 50 grids, identification is also eliminated. This identification considers the possibility of combining several cloud clusters to one cluster in current image, but is out of consideration of separating.

4.4 Cloud discrimination

MLUA detection

The condition for thick cloud areas reaching the tropopause as MLUAs is stricter than that for thick cloud areas

$\{\mathrm{thr}_1^{\varepsilon_{trp}} < \varepsilon_{trp}$ or $(\mathrm{thr}_2^{\varepsilon_{trp}} < \varepsilon_{trp}$ and $\mathrm{thr}^{R} < \mathrm{R(Band\ 03)})$

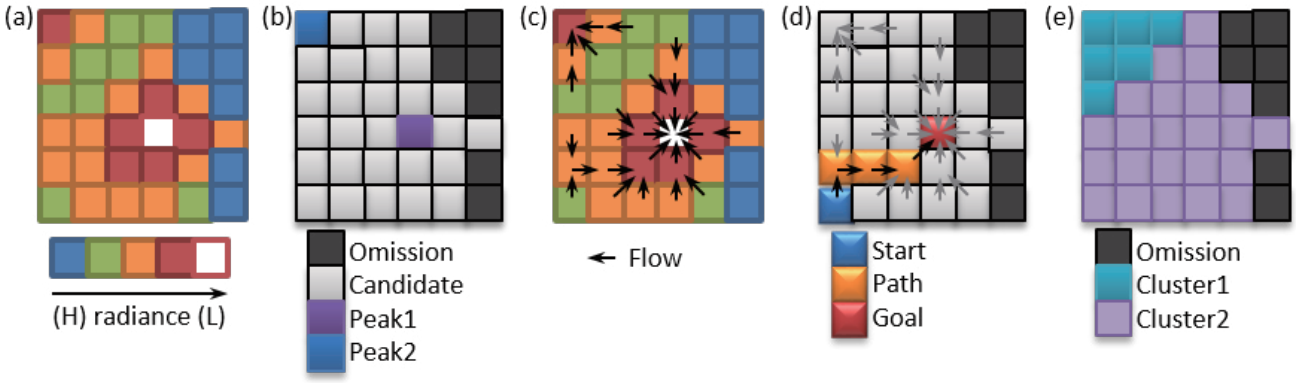

Fig. 11 Cloud clustering concept. (a) Radiance fields. (b) Local minimum radiances are considered as "peak" grids. Temporal cluster numbers are assigned at peaks and reserved as C^C. (c) Search of "flow" to identify the steepest radiance gradient. (d) Flow tracing from the bottom left of the grid to to a peak. (e) All grids on the way to the peak based on flow tracing are assigned to the same cluster number of the peak, reserved as C^C, and are regarded as a cloud cluster.

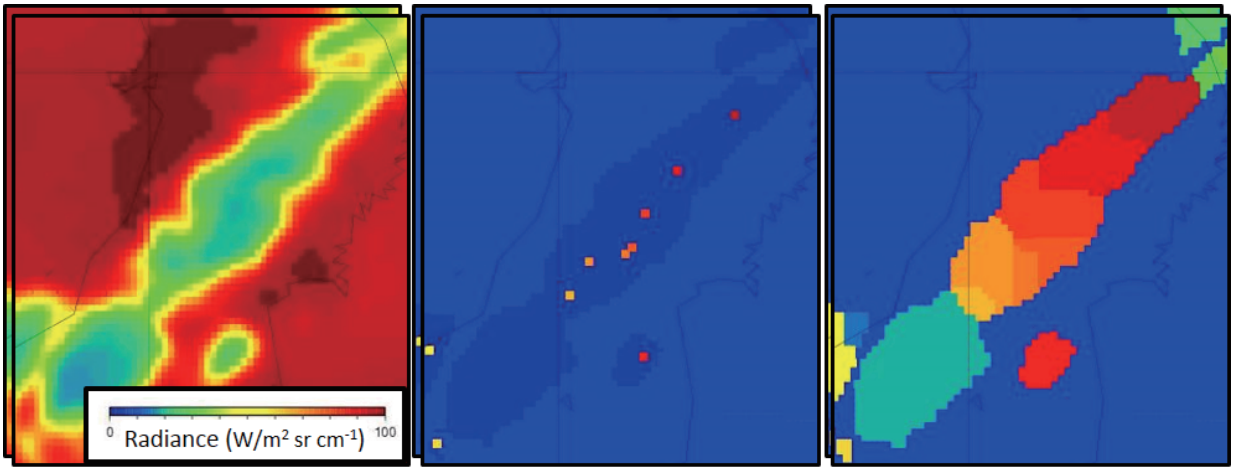

Fig. 12 Smoothed radiance fields (left), detected local minima of radiance (center) and cloud clusters after flow tracing (right).

$$\text{or } (\text{thr}_2^{\varepsilon_{\text{trp}}} < \varepsilon_{\text{trp}} \text{ and "the destination of previous detection"})\}$$
$$\text{and } \beta(\text{Band 15}/\text{Band 13}) < \text{thr}^{\beta}, \qquad (13)$$

where, thr^{R} is the detection threshold for Band 03 reflectivity (Fig. 10) and the condition "the destination of previous detection" represents grids of previous MLUAs in consideration of cloud cluster movement to mitigate the discontinuity from the previous detection.

CB detection

CB is detected in grids within CB candidate where Band 13 BT is less than the boundary BT, except in decaying cloud cluster. Fig 13 shows a conceptual image of CB detection.

In estimation of the boundary BT between a protrusion area and other areas, the intermediate BT T^m in a cloud cluster is calculated from the minimum BT T^t and the BT of the basis around the protrusion $T^b(t)$, which is estimated as the averaged BT of the MLUA in a cloud cluster. If the cloud cluster is identified with the previous ones, $T^b(t)$ is temporally averaged with past cloud clusters. This is estimated by weighted averaging in consideration of the time series from the current time described as,

$$\overline{T^b} = \sum_{t'=t-5}^{t} T^b(t')\,w(t') \Big/ \sum_{t'=t-5}^{t} w(t'),$$

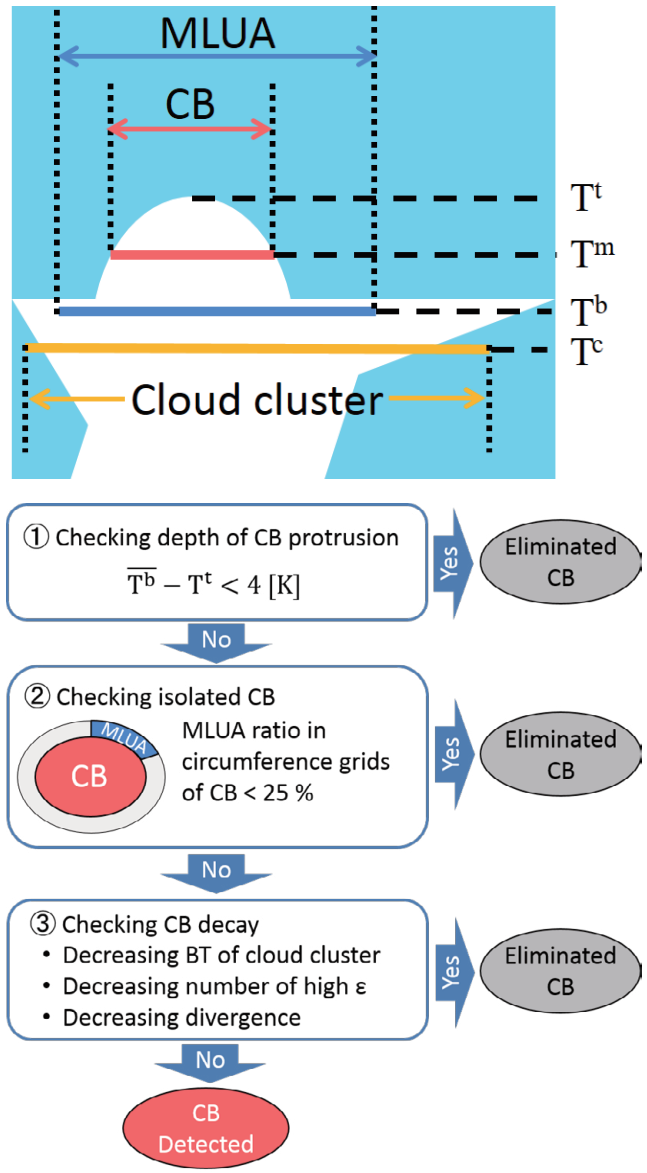

Fig. 13 Conceptual image of CB (top) and the flow of elimination of CB detection (bottom).

$$w(t') = \exp\left[-\frac{\{mn(t) - mn(t')\}^2}{\sigma_t^2}\right], \qquad (14)$$

where, up to past 5 images are used in this smoothing process. This averaging period is about 30 minutes based on the isolated cumulonimbus lifetime. This smoothing process mitigate the temporal variation of the basis around the protrusion.

The boundary BT is the average of the minimum BT and the BT of basis around protrusion according to

$$T^m = \frac{\overline{T^b} + T^t}{2}. \qquad (15)$$

In a cloud cluster, grids whose BT exceeds the boundary BT T^m are defined as CB.

Elimination of CB detection

CB detection is eliminated if the cloud cluster meets the conditions outlined below.

① Depth of CB protrusion

According to research involving the overshooting top product for GOES-R (Bedka et al., 2011), the difference between the BT for 10.8 μm at the top of a protrusion and that of anvil cloud is more than 6.5 K with typical lively cumulonimbi. In the study, many cumulonimbi in the tropics were particularly noted. However, as this product is designed based on mid-latitude region (Japan area), if the difference between $\overline{T^b}$ and T^t is less than 4 K on the safe side, CB detection is eliminated.

② Isolated CB

Investigation of various events has indicated that almost CB in the early convective stage accompanies MLUA, while many in the decaying stage not. Accordingly, if the ratio of the number of CB circumference contacts with MLUA among all circumference grids is less than 25 %, CB detection is eliminated.

③ CB decay

Monitoring the time series of various types of cloud cluster information allows the elimination of decaying CB. The evaluating parameters are acquired as the temporal rate of change in Band 13 BT, the ratio of high effective emissivity and divergence in cloud clusters. The temporal rate of change for every parameter can be expressed by

$$\Delta V(t) = V(t) - V(t-1), \qquad (16)$$

where, V represents each parameter calculated for a temporal rate of change. This evaluation process requires temporal smoothed data from the last five images. It mitigates uncertainness caused by cloud clustering and identification processes. The time series for each parameter $\overline{\Delta V}$ is determined using equation (14) in which $T^b(t)$ is exchanged for $\Delta V(t)$.

First, decaying CB is estimated from the time series of Band 13 BT as the averaging cloud cluster BT T^c, the

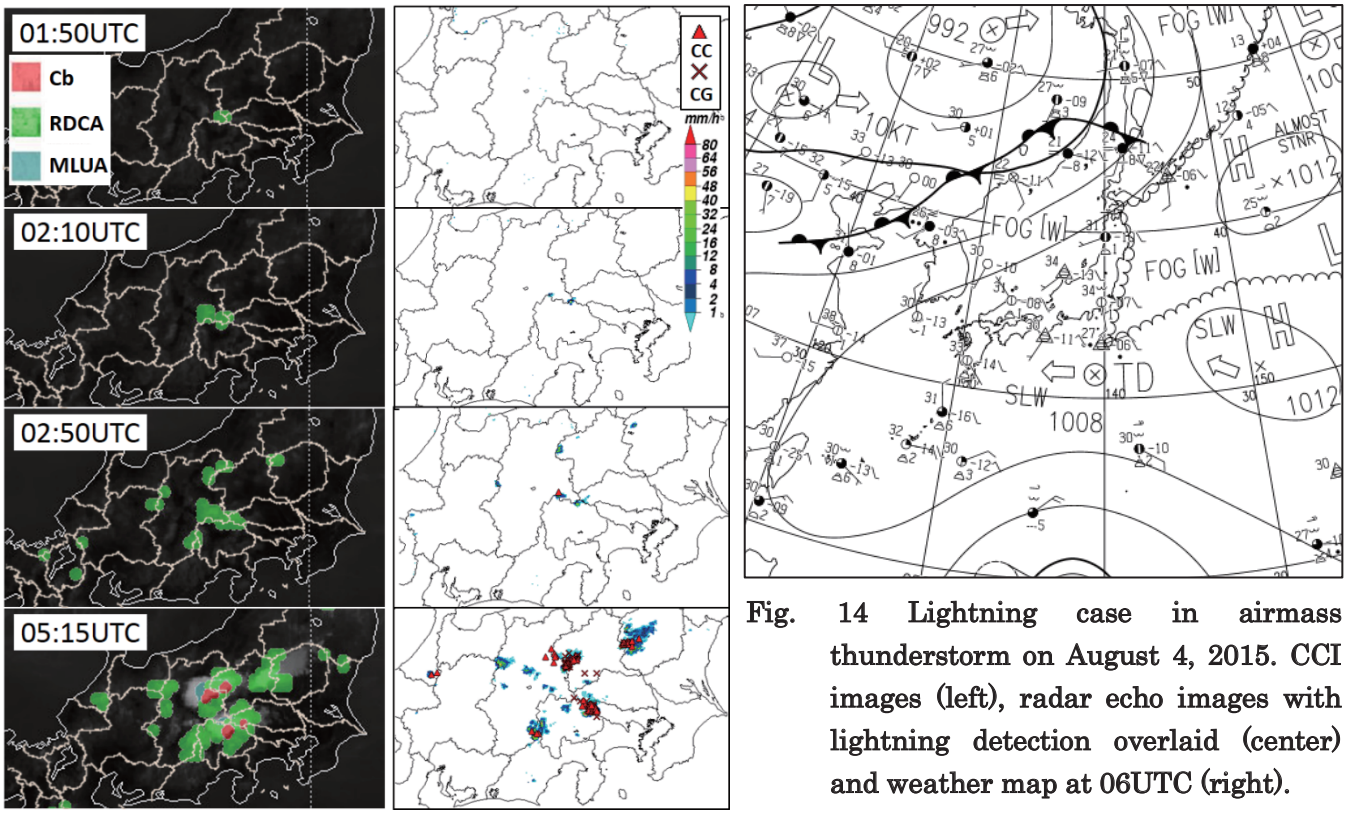

Fig. 14 Lightning case in airmass thunderstorm on August 4, 2015. CCI images (left), radar echo images with lightning detection overlaid (center) and weather map at 06UTC (right).

basis BT around the protrusion T^b and the minimum BT T^t. If it meets the following condition (17), the CB detection is eliminated because CB in the cloud cluster is considered to be decaying.

$$\overline{\Delta T^c} > 0 \text{ or } \overline{\Delta T^t} > 0 \text{ or } \overline{\Delta T^t - \Delta T^b} > 0. \quad (17)$$

Next, the ratios of the number of grids with effective emissivity exceeding 0.9 and 0.8 to total grids in a cloud cluster are defined as N^{ε_1} and N^{ε_2}, respectively. If they meet the following condition (18), CB detection is eliminated.

$$\overline{\Delta N^{\varepsilon_1}} < 0 \text{ or } \overline{N^{\varepsilon_2}} < 0. \quad (18)$$

Finally, decreasing divergence div(v) as mentioned in Section 4.2 indicates a shrinking cloud cluster. Hence, if it meets the following condition (19), CB detection is eliminated.

$$\overline{\Delta \mathrm{div}(v)} < 0. \quad (19)$$

5. Case studies

This chapter covers case studies relating to CCI performance and validation of RDCA.

5.1 Early detection of lightning in an airmass thunderstorm (August 4, 2015)

Fig. 14 shows CCI images, radar echo images with lightning detections overlaid and a weather map (06 UTC) for a period of intense lightning in Japan's Kanto region on August 4, 2015. Typhoon 1513 (Soudelor), located over the Pacific Ocean south of Japan, increased temperature around Japan in association with Pacific High, causing extreme daytime lightning. The first RDCA was detected in a mountainous region of Kanto at 01:50 UTC. The first radar echo was detected 20-minute later at 02:10 UTC, and the first lightning was observed at 02:50 UTC. In the afternoon (05:15 UTC), these lightning areas were detected as CB, which was consistent with the lightning detection. This case highlights how CCI product provides helpful information relating to rapid cumulus development for areas without upper-level cloud under high-pressure systems.

5.2 False detection of RDCA (July 25, 2016)

The infrared-visible observation is limited in terms of presuming internal cloud structures. Fig. 15 shows a case

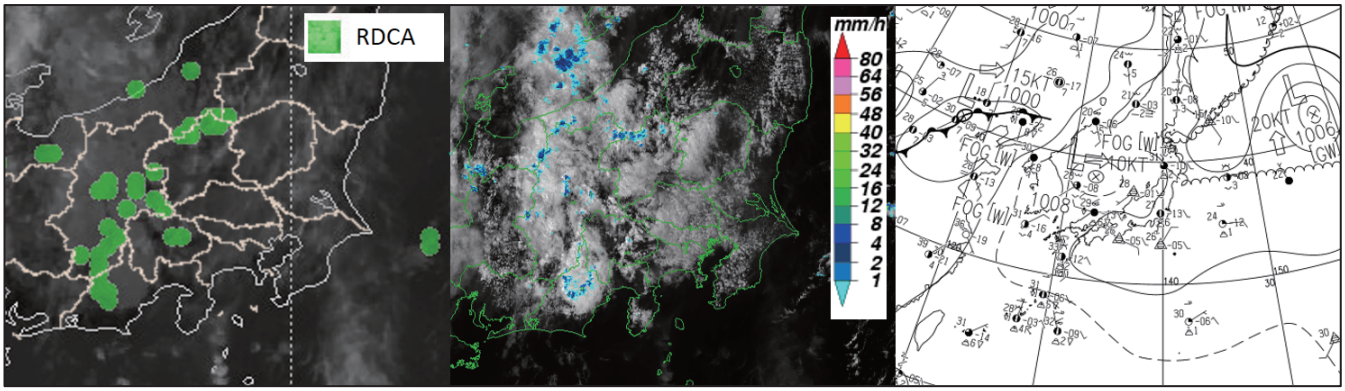

Fig. 15 Error detection case with lower and upper layer cloud present on July 25, 2016. CCI image (left), visible image with radar echo overlaid (center) and weather map at 06 UTC (right).

Table 4 RDCA detection contingency table.

		Observed Lightning		Total
		Yes	No	
Forecast (RDCA)	Positive	a/aa: Hit	b: False alarm	a+b : # of RDCA
	Negative	c: Miss	d	
Total		aa+c: # of lightning		

in which numerous RDCAs were falsely detected due to thin upper-level cloud passing over low-level cloud on July 25, 2016. The weather map indicated that a low-pressure system over the Sea of Japan was moving east. Cumuli with a weak developing trend were present in front of the depression, and no lightning was detected around the Kanto area. False detection of RDCAs was likely attributable to thin upper-level cloud passing over low-level cloud, which appeared as cloud development (thin cloud could be seen in visible imagery animation, but was hard to almost indiscernible from single still images). Thus, erroneous detection can occur when upper-level cloud covers low-level cloud.

5.3 RDCA evaluation

RDCA accuracy is evaluated for cases in which LIDEN detects CC/CG lightning. The contingency table (see Table 4) is used for evaluation. Two types of “Hit” are defined as follows for simple consideration of cloud movement and expansion.

a: In case that lightning is observed in one grid around RDCA (0.1 degree grid squares) within 60 minutes of the RDCA’s detection.

aa: In case that RDCA was detected in one grid around lightning detection (0.1 degree grid squares) from 60 minutes downward before lightning is observed.

Multiple RDCAs or lightning detections in the same cloud mass at different times are considered independent.

RDCA accuracy is calculated from the probability of detection (POD) and the false alarm ratio (FAR) as

$$\mathrm{POD} = {}^{\mathrm{aa}}/_{(\mathrm{aa}+\mathrm{c})},$$

$$\mathrm{FAR} = {}^{\mathrm{b}}/_{(\mathrm{a}+\mathrm{b})}. \qquad (20)$$

Fig. 16 shows a daily chart of POD, FAR, and the number of lightning observation in August, 2016. As LR analysis is maintained for summertime airmass thunderstorms, RDCAs were detected accurately in early August when lightning brought by such storms was common. However, accuracy decreased in late August, especially with high FAR, as a result of numerous false detections associated with frequent typhoon passage over Japan and cloud masses covering large parts of the country. Table 5 also shows the monthly total accuracy in August, 2016 for daytime (00 - 09 UTC), nighttime (12 - 21 UTC), and all-day (00 - 23 UTC). Daytime accuracy is higher than that at nighttime because Band 03 indicators are available only during the daytime.

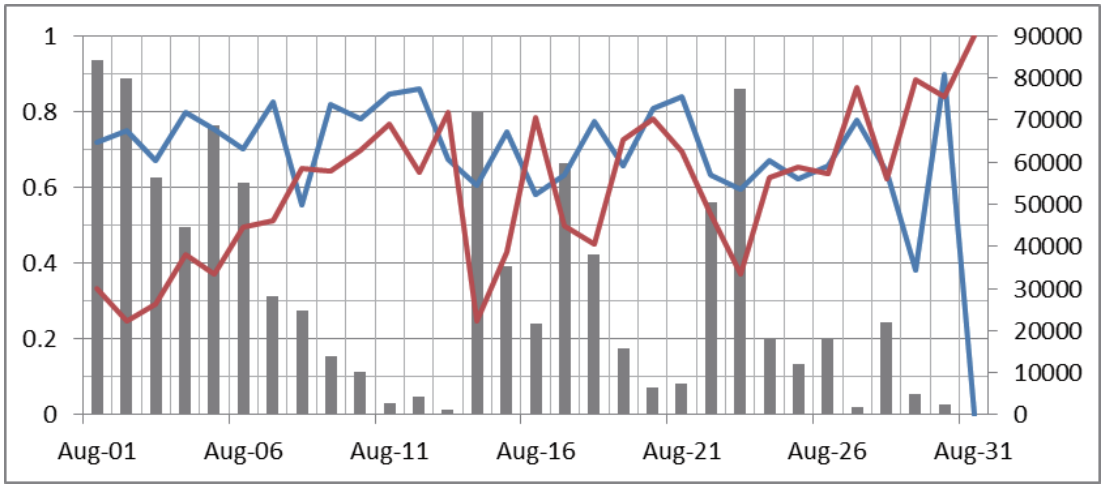

Fig. 16 Daily accuracy chart for RDCA and numbers of lightning occurrence in August of 2016. Cyan line is POD, red line is FAR (left axis) and gray bars are numbers of lightning occurrence (right axis).

Table 5 Monthly accuracy rate and numbers of lightning occurrence in August of 2016.

	POD	FAR	# of lightning
All day (00-23UTC)	0.691	0.551	936,087
Day time (00-09UTC)	0.743	0.548	455,428
Night time (12-21UTC)	0.633	0.559	315,301

6. Conclusion

MSC/JMA has developed the CCI product which identifies RDCAs, CBs and MLUAs. The CCI product leverages the high temporal and multi-spectral data from Himawari-8 to detect various cloud areas ranging from developing cumulus to mature cumulonimbus. RDCA identification in particular helps to monitor cumulus areas that could potentially cause lightning earlier than ground observation and weather radar, and improves on the algorithm for MTSAT-1R RSO by enabling nighttime detection. The product is also intended to support aviation safety. However, RDCA can result in false detections and misses when upper-level cloud passes over low-level cloud, and are also processed separately from CB and MLUA detection, making consistent cloud area detection difficult. Resolutions of these problems involve the incorporation of various types of information from NWP data and radar observation, and require sophisticated methods relating to cloud mask and cloud tracking. The successive cloud detection is also needed to clarify the process of cumulonimbus development. In future work, wide-ranging detections for CCI from Himawari-8 FD observation (despite a temporal resolution lower than that of Japan area observation) will be developing to address a significant need for cumulonimbus detection in tropical regions.

Reference

Ackerman, S. A., 1996: Global Satellite Observations of Negative Brightness Temperature Difference between 11 and 6.7 μm, *J. Atoms. Sci.*, **53**, 2803-2812.

Bedka K., J. Brunner, and W. Felts, 2011: Overshooting top and Enhanced-V Detection, NOAA NESDIS Center for Satellite Application Research Algorithm Theoretical Basis Document.

Bessho, K., K. Date, M. Hayashi, A. Ikeda, T. Imai, H. Inoue, Y. Kumagai, T. Miyakawa, H. Murata, T. Ohno, A. Okuyama, R. Oyama, Y. Sasaki, Y. Shimazu, K. Shimoji, Y. Sumida, M. Suzuki, H. Taniguchi, H. Tsuchiyama, D. Uesawa, H. Yokota, and R. Yoshida, 2016: An Introduction to Himawari-8/9 – Japan's new-generation geostationary meteorological satellites. *J. Meteor. Soc. Japan*, **94**, doi:10.2151/jmsj.2016-009.

Eyre, J. R., 1991: A fast radiative transfer model for satellite sounding systems. *ECMWF Tech. Memo.* **176**, 28pp.

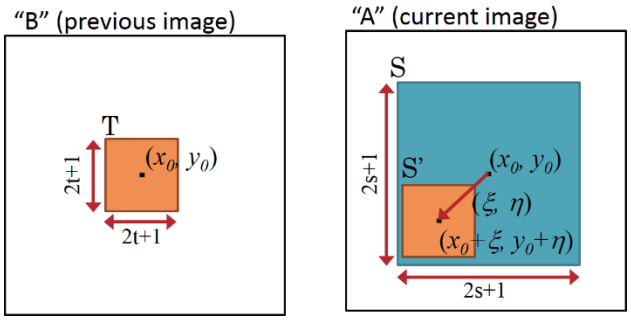

Fig. A-1 Template area and search area for cloud motion tracking.

Inoue, T., 1987: An instantaneous delineation of convective rainfall area using split window data of NOAA-7 AVHRR. *J. Meteor. Soc. Japan*, **65**, 469-481.

Matthee, R., and J. R. Mecikalski, 2013: Geostationary infrared methods for detecting lightning-producing cumulonimbus clouds, *J. Geophys. Res. Atmos.*, **118**, 6580-6592, doi:10.1002/jgrd.50485.

Mecikalski, J. R., and K. M. Bedka, 2006: Forecasting convective initiation by monitoring the evolution of moving convection in daytime GOES imagery, *Mon. Wea. Rev.*, **134,** 49-78.

MSC/JMA, 2000: Analysis and Use of Meteorological Satellite Image. Meteorological Satellite Center, 161 pp (in Japanese).

Okabe, I., T. Imai, and Y. Izumikawa, 2011: Detection of Rapidly Developing Cumulus Areas through MTSAT Rapid Scan Operation Observation, *Meteorological Satellite Center technical note,* **55,** 69-92.

Pavolonis, M, 2010 : GOES-R Advanced Baseline Imager (ABI) Algorithm Theoretical Basis Document for Cloud Type and Phase, NOAA NESDIS CENTER for SATELLITE APPLICATION RESERCH Algorithm Theoretical Basis Document.

Siewert, C. W., M. Koening, and J. R. Mecikalski, 2010: Application of Meteosat second generation data towards improving the nowcasting of convective initiation. *Meteor. Appl.*, **17**, 442-451, doi:10.1002/met.176.

Zinner, T., H. Mannstein, A. Tafferner, 2008: Cb-TRAM: Tracking and monitoring severe convection from onset over rapid development to mature phase using multi-channel Meteosat-8 SEVIRI data, *Meteorol Atmos Phys.*, **101**, 191–210, doi:10.1007/s00703-008-0290-y.

Appendix A Cloud motion tracking

Cloud motion tracking is adopted in the inter-correlation method, which involves the use of correlation coefficient as a function to evaluate similarities between the current image "A" and the previous image "B". Two areas are defined in cloud tracking for motion cancellation:

① An area in which cloud features are defined on clipping image "B" for cloud tracking (Template area: T)

② The search range on image "A" to compare the template area defined as ① (Search area: S)

Fig. A-1 shows illustrations of each area. The template and search areas are (2t+1) and (2s+1) grid squares in size, respectively. A template area centered (x_0, y_0) on image "B" is expressed by

$$\mathrm{T}(i,j) = \mathrm{V_B}(x_0 + i, y_0 + j); \quad -\mathrm{t} \le i \le \mathrm{t}, -\mathrm{t} \le j \le \mathrm{t}. \qquad (\mathrm{A.1})$$

The search area on image "A" with the same center (x_0, y_0) is given as

$$\mathrm{S}(\xi,\eta) = \mathrm{V_A}(x_0 + \xi, y_0 + \eta); \quad -\mathrm{s} \le \xi \le \mathrm{s}, -\mathrm{s} \le \eta \le \mathrm{s}. \qquad (\mathrm{A.2})$$

The template area for the candidate destination is cut out as clipping image S' at the center (ξ,η) on the search area, given by

$$\mathrm{S'_{(\xi,\eta)}}(i,j) = \mathrm{S}(\xi + i, \eta + j); \quad -\mathrm{t} \le i \le \mathrm{t}, -\mathrm{t} \le j \le \mathrm{t}. \qquad (\mathrm{A.3})$$

The field of inter-correlation coefficient $\mathrm{C}(\xi,\eta)$ between T and S' is given by

$$\mathrm{C}(\xi,\eta) = \frac{\sum_{i=-\mathrm{t}}^{\mathrm{t}}\sum_{j=-\mathrm{t}}^{\mathrm{t}}\{\mathrm{T}(i,j) - \overline{\mathrm{T}}\}\{\mathrm{S'_{(\xi,\eta)}}(i,j) - \overline{\mathrm{S'_{(\xi,\eta)}}}\}}{\sqrt{\sum_{i=-\mathrm{t}}^{\mathrm{t}}\sum_{j=-\mathrm{t}}^{\mathrm{t}}\{\mathrm{T}(i,j) - \overline{\mathrm{T}}\}^2}\sqrt{\sum_{i=-\mathrm{t}}^{\mathrm{t}}\sum_{j=-\mathrm{t}}^{\mathrm{t}}\{\mathrm{S'_{(\xi,\eta)}}(i,j) - \overline{\mathrm{S'_{(\xi,\eta)}}}\}^2}},$$

$$\overline{\mathrm{T}} = \frac{1}{(2\mathrm{t}+1)^2}\sum_{i=-\mathrm{t}}^{\mathrm{t}}\sum_{j=-\mathrm{t}}^{\mathrm{t}}\mathrm{T}(i,j),$$

$$\overline{\mathrm{S'_{(\xi,\eta)}}} = \frac{1}{(2\mathrm{t}+1)^2}\sum_{i=-\mathrm{t}}^{\mathrm{t}}\sum_{j=-\mathrm{t}}^{\mathrm{t}}\mathrm{S'_{(\xi,\eta)}}(i,j). \qquad (\mathrm{A.4})$$

The maximum point $(\hat{\xi},\hat{\eta})$ of $\mathrm{C}(\xi,\eta)$ is extracted to

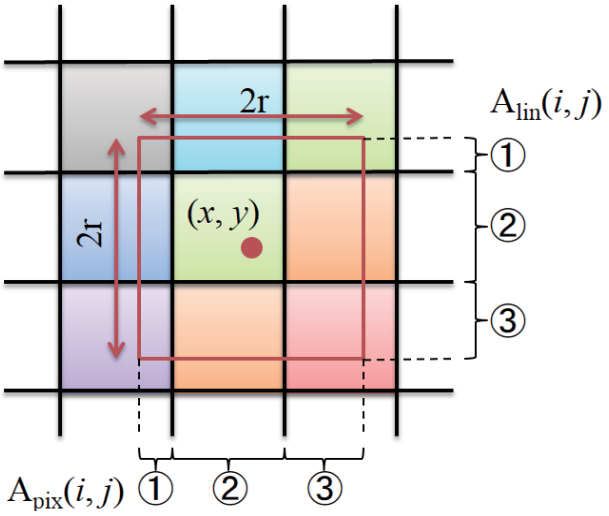

Fig. B-1 Area calculation for factor ρ exceeding one.

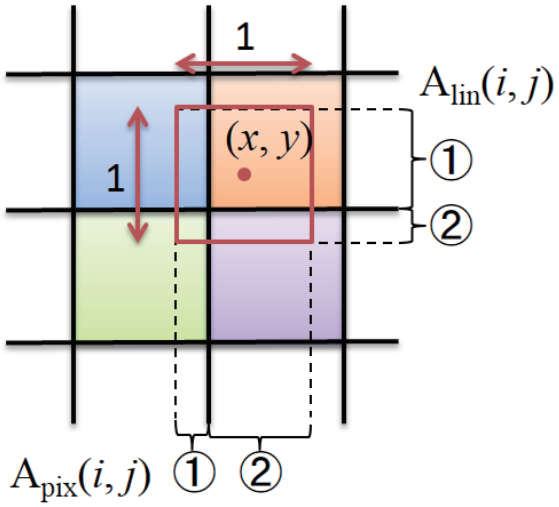

Fig. B-2 Area calculation for factor ρ less than one.

determine cloud motion, and the grid (x_0, y_0) on image "B" are identified with the relevant grid $(x_0 + \hat{\xi}, y_0 + \hat{\eta})$ on image "A".

This method involves the assumption that information on the template area (i.e., cloud features) changes little between the two images, and tracking may be inaccurate as a consequence of big temporal changes such as developing cumulus/cumulonimbus. However, such effects are ignored in this product because of the short interval between images (5 minutes).

Appendix B Spatial interpolation

This outlines spatial interpolation from original grid squares to new ones with ρ times resolution.

Fig. B-1 shows a case that factor ρ is greater than one. The data for new grid square $\bar{V}(x,y)$ with the center at (x, y) (shown in red square in Fig. B-1) is set as the weighted average of original data $V(i,j)$ (shown in black squares in Fig. B-1) contained in the new grid squares. The weighting factor is allocated on the ratio of each area of the original grid $A(i,j)$ in the new grid. With this, provided that $\rho = 2r$, $\bar{V}(x,y)$ can be expressed as

$$\bar{V}(x,y) = \frac{\sum_{i=\mathrm{int}(x-r)}^{\mathrm{int}(x+r)} \sum_{j=\mathrm{int}(y-r)}^{\mathrm{int}(y+r)} A(i,j) \times V(i,j)}{\sum_{i=\mathrm{int}(x-r)}^{\mathrm{int}(x+r)} \sum_{j=\mathrm{int}(y-r)}^{\mathrm{int}(y+r)} A(i,j)},$$

$$A(i,j) = A_{pix}(i,j) \times A_{lin}(i,j),$$

$$A_{lin}(i,j) = \begin{cases} 1 - [y + r - \mathrm{int}(y + r)] & \cdots ①\ \mathrm{int}(y - r) = j \\ 1 & \cdots ②\ \mathrm{int}(y - r) < j < \mathrm{int}(y + r) \\ y + r - \mathrm{int}(y + r) & \cdots ③\ \mathrm{int}(y + r) = j \end{cases},$$

$$A_{pix}(i,j) = \begin{cases} 1 - [x + r - \mathrm{int}(x + r)] & \cdots ①\ \mathrm{int}(x - r) = i \\ 1 & \cdots ②\ \mathrm{int}(x - r) < i < \mathrm{int}(x + r) \\ x + r - \mathrm{int}(x + r) & \cdots ③\ \mathrm{int}(x + r) = i \end{cases}.$$

(B.1)

Where, int() expresses a function for conversion from a value to an integer. $A_{lin}(i,j)$ and $A_{pix}(i,j)$ are line/pixel lengths in the original grid. As shown in Fig. B-1, these are equal to one if the original grid does not contain squares at the edge of the new grid (② in Fig. B-1), and are not equal to one if the original grid contains squares at the edge (① and ③ in Fig. B-1).

Fig. B-2 shows a case that factor ρ is not greater than one. Line/pixel lengths of the new grid are set as one with the center at (x, y) on the same scale as the original grid, which corresponds to $r = 1/2$ in Equation (B.1). Here, line/pixel lengths in the original grid $A_{lin}(i,j)$, $A_{pix}(i,j)$ depend on the position of the original (i, j) in the new grid. These take the following values in the ① and ② in Fig. B-2:

$$A_{lin}(i,j) = \begin{cases} 1 - [y + 1/2 - \mathrm{int}(y + 1/2)] & \cdots ①\ \mathrm{int}(y - 1/2) = j \\ y + 1/2 - \mathrm{int}(y + 1/2) & \cdots ②\ \mathrm{int}(y + 1/2) = j, \end{cases}$$

$$A_{pix}(i,j) = \begin{cases} 1 - [x + 1/2 - \mathrm{int}(x + 1/2)] & \cdots ①\ \mathrm{int}(x - 1/2) = i \\ x + 1/2 - \mathrm{int}(x + 1/2) & \cdots ②\ \mathrm{int}(x + 1/2) = i. \end{cases}$$

(B.2)

積乱雲情報プロダクトアルゴリズム

隅田　康彦*、鈴江　寛史*、今井　崇人**、傍嶋　明***

要旨

2015 年 7 月に運用を開始したひまわり 8 号は 10 分間隔のフルディスク観測と同時に日本周辺において 2.5 分間隔の高頻度な観測を実施している。気象衛星センターでは、この日本域観測を利用して、積乱雲情報プロダクトを提供している。本プロダクトは、発雷をもたらすような急速に発達する積雲（積雲急発達域）、積乱雲域及びかなとこ巻雲域（中下層雲不明域）からなり、航空機の安全運航に供するデータを提供している。本報告では、これら積乱雲情報プロダクトの各要素の検出アルゴリズムについて記述する。

*気象衛星センターデータ処理部システム管理課

**気象庁観測部観測課観測システム運用室

***気象庁予報部予報課

（2016 年 9 月 16 日受領、2016 年 12 月 14 日受理）